Fractological investigations on the fracture in concrete

V.Mechtcherine & H.S.Müller
University of Karlsruhe, Karlsruhe, Germany

ABSTRACT: The fracture mechanical properties, in particular uniaxial tensile strength f_t, Young's modulus E_0 and fracture energy G_F as well as the shape of the stress-strain and the stress-deformation relations were investigated for ordinary and high-strength concrete. In order to analyse failure mechanisms of these concretes, the roughness and the fractal dimension of the entire fracture surfaces and of their components (fractured aggregate, cement paste and cement paste-aggregate interface) were calculated. These data showed a clear correlation with fracture properties of the concretes investigated. Further, the mechanisms of the transfer of tensile stress across the crack were studied numerically. Hereby, a new method was applied to generate artificial concrete failure surfaces with a given fractal dimension. The results of the FE simulations confirmed the experimentally found correlations between the condition of the failure surface and the fracture mechanical properties of the investigated concretes.

1 INTRODUCTION

In recent years fracture surfaces became an object of intensive research for better understanding of the phenomena of crack formation and propagation in concrete. However, the effects of nearly all relevant parameters (with exception of the maximum grain size (Mihashi et al. 1994) as well as of the temperature and the strain rate (Mechtcherine et al. 1995)) on the energy consumption of a discrete crack are still unknown. Further, it should be investigated, how the information about the condition of the fracture surfaces can be used for the modeling of the fracture behavior of concrete.

In this study the effects of the concrete strength and the curing conditions on the formation and propagation of cracks in concrete were investigated. First, a series of deformation controlled uniaxial tension tests with different set-ups were performed for normal strength concrete (NSC) and high-strength concrete (HSC). From the test data the characteristics of the material response, i.e. uniaxial tensile strength f_t, Young's modulus E_0 and specific fracture energy G_F were evaluated.

As the second step, the entire fracture surfaces of the tested specimens were studied by means of optical analyses in order to understand fracture mechanisms and to explain the effect of the parameters under investigation on the fracture energy G_F and on the shape of the stress-crack opening diagrams (σ-w relations) derived from the tests on notched specimens. Furthermore, the components of the failure surfaces – fractured aggregate, cement paste and cement paste-aggregate interface – were investigated to provide additional information about the local failure mechanisms in concrete. These data were correlated with the shape of the stress-strain curves (σ-ε relations) obtained from the experiments on unnotched prisms.

Finally, a new method was applied to generate artificial fracture surfaces of concrete with a fractal dimension as obtained from the fractological investigations. These artificial surfaces were applied for the FE analysis of the mechanisms of the stress transfer over discrete cracks.

2 FRACTURE MECHANICAL EXPERIMENTS

2.1 *Experimental program, preparation of specimens and test set-up*

The composition of the two types of concrete which were investigated is given in Table 1. In both mixtures ordinary Portland cement CEM I 32.5 R was used. As aggregate quartzite Rhine sand and gravel were applied. The mixture for the HSC had a silica fume content of 45 kg/m³. By adjusting the dosage of a sodium naphthalene sulfonate type superplasticizer the same nominal spread (43 – 47 cm) for the both types of concrete could be achieved. Their compressive strength obtained from the tests on cube specimens at an age of 28 days was 96 MPa and 44 MPa, respectively.

Table 1: Composition of the concretes

Concrete	w/c	Cement²	SF	Aggregate 0-16 mm	SP	f_{cc}^{cube}
		[kg/m³]	[kg/m³]	[kg/m³]	[kg/m³]	[MPa]
HSC	0.33	450	45	1721	21	96
NSC	0.6	318	-	1811	1	44

SF = Silica Fume   SP = Super Plasticiser

Dog-bone shaped prisms with a gauge length of 250 mm were chosen to determine the uniaxial tensile strength f_t, the tangent modulus of elasticity E_0, as well as the σ-ε diagram for increasing stresses (see Fig. 1, left). Notched prisms were used to determine fracture energy G_F and the complete stress-deformation relation. Both types of specimens had the same effective cross-section 60×100 mm². A schematic view of the specimen geometries and typical stress-deformation relations are given in Figure 1 (right). Details may be found in (Mechtcherine 2000).
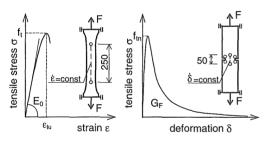

Figure 1. Schematic view of the geometry of dog-bone (left) and notched (right) specimens with typical stress-deformation relations (geometrical data in [mm])

All specimens were cast horizontally in metal forms. After demoulding, the specimens were wrapped in a thin plastic sheet to which an aluminium foil was glued in order to protect the concrete against desiccation. For the normal strength concrete under investigation also a parallel series of specimens were stored, after demoulding, unsealed in a climatic chamber at a relative humidity of 65 % and a temperature of 23 °C. All specimens were tested at an age of 56 days.

To assure a stable and possibly symmetrical crack propagation in the uniaxial tension tests, stiff metal plates were glued to the specimens. Finally the metal plates were firmly connected with the bearing platens of the testing machine.

In the tests on the dog-bone shaped prisms the strain rate was controlled by means of the average signal of two LVDTs fixed to the specimens. In the experiments on the notched specimens four LVDTs with a gauge length of 25 mm were placed on the notch tips on both sides of the specimen to achieve a better deformation rate control. Two further LVDTs with a gauge length

of 50 mm were placed in the middle of the notched cross-section to provide the data for the σ-δ relation (see Fig. 1, right).

The tension tests on dog-bone shaped specimens were performed with a strain rate $\dot{\varepsilon}$ of 10^{-6} 1/s. The corresponding deformation rate $\dot{\delta}$ in the tension tests on notched specimens was $5 \cdot 10^{-5}$ mm/s.

2.2 Experimental results on strength and fracture behavior

The ascending stress-strain relation for concrete subjected to uniaxial tension has a characteristic shape as shown in the Figure 1 (left). While the relation is linear at low stresses the shape of the curve deviates from the linearity at higher stresses due to the microcrack formation, until it becomes horizontal at $\sigma = f_t$. A stable crack propagation could not be achieved with the particular test set-up used here.

According to Table 2, the tensile strength f_t, the tangent modulus of elasticity E_0 and the strain ε_{tu} (the strain at peak stress $\sigma = f_t$) of the HSC are significantly higher than the corresponding values for the NSC. The unsealed normal strength concrete showed lower f_t- and E_0-values, and slightly lower values of the strain ε_{tu} than the sealed NSC.

In the uniaxial tension tests on notched specimens also the descending branch of the σ-δ relation could be determined up to nearly complete separation of the specimens into two parts because of the localized crack due to the notches and the reduction of the gauge length for the control of deformation rate to 25 mm. The values of the net tensile strength f_{tn}, the fracture energy G_F and the characteristic length l_{ch} obtained from these experiments are listed in Table 2.

The net tensile strength f_{tn} shows a similar dependence on the concrete composition and the curing conditions as the tensile strength f_t measured on the dog-bone specimens, however f_{tn} is lower than f_t, indicating a notch sensitivity of the concretes.

Table 2. Results of the uniaxial tension tests

Concrete	f_t [MPa]	E_0 [MPa]	ε_{tu} [$\cdot 10^{-3}$]	f_{tn} [MPa]	G_F [N/m]	l_{ch} [m]
HSC	6.1 (0.2)	47700 (170)	0.151 (0.005)	5.4 (0.7)	162 (21)	0.21
NSC sealed	3.8 (0.4)	36320 (1540)	0.130 (0.009)	2.9 (0.3)	135 (21)	0.34
NSC unsealed	3.1 (0.2)	33060 (750)	0.128 (0.01)	2.7 (0.4)	167 (24)	0.57

Standard deviations are given in parentheses.

The fracture energy G_F is defined as the energy per unit area needed for complete separation of a specimen into two parts. This value corresponds to the area under the σ-δ relation. The fracture energy

of the high-strength concrete is higher than the corresponding value of the sealed normal strength concrete, but slightly lower than the fracture energy of the unsealed normal strength concrete.

The characteristic length l_{ch} ($l_{ch} = G_F \cdot E_0/f_t^2$) decreases with increasing strength of concrete. The specimens made of the NSC and protected from desiccation showed a smaller characteristic length than those of the unsealed concrete. The higher l_{ch}-values indicate a more ductile behaviour of concrete.

3 QUANTIFICATION OF THE CONDITION OF THE FRACTURE SURFACES

3.1 Projected fringes technique

To study the effect of the concrete strength and the curing conditions on the crack propagation the fracture surfaces from the uniaxial tension test were measured using the projected fringes technique (see Fig. 3). Height differences of the surface induce a lateral displacement of the projected strip pattern. The incorporation of geometrical data of the optical configuration then allows the contour information to be detected from the phase shift of the surface strip pattern at each surface location (Wolf et al. 1996).

The measurement at intervals of 0.16 mm gives 375×625 mesh data for each failure surface. Typical contours of a fracture surface of the HSC and the NSC, sealed and unsealed, are shown in Figure 2.
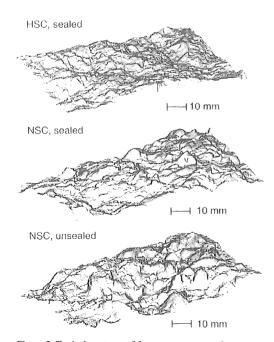

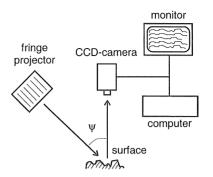Figure 2. Typical contours of fracture concrete surfaces

Figure 3. Principle of the projected fringes technique

3.2 Confocal microscope technique

To study the condition of the components of the fracture surfaces the confocal microscope technique was applied. In the confocal microscope a point source is imaged in the fracture surface plane. The light reflected by the surface is directed to a photo-multiplier via a small aperture (Fig. 4), which physically excludes light coming from above and below the focal plane of the microscope objective. Laser light reflected from a dichroic mirror into a scanning device moves in a defined raster in a x-y plane. The arrangement of the detector aperture ensures that only information from the focal plane reaches the detector. By coupling a step motor to the focusing unit and changing the focal plane, whole series of sectional images of the fracture surfaces could be performed. Three-dimensional images of the investigated surfaces were rebuild then by overlaying the images of section series.
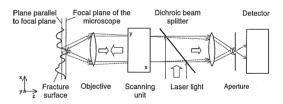

Figure 4. Basic concept of a confocal laser scanning microscope after Wilson (1990)

In this study 512×512 mesh data have been used for each monitored spot of 0.64×0.64 mm². Typical contours of the fracture surfaces of cement paste and cement paste-aggregate interface of the sealed normal strength concrete are shown in Figure 5.

3.3 Determination of the roughness and the fractal dimension

From the optical measurement data the roughness and the fractal dimension of the surfaces were determined
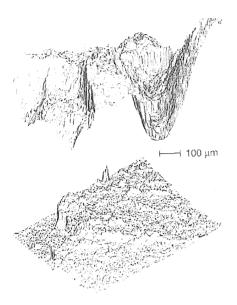
83

Figure 5. Typical contours of the fracture surfaces of cement paste (above) and cement paste-aggregate interface (below)

in order to quantify the condition of the entire fracture surfaces as well as of their components.

The roughness R_S of the entire fractured surface was calculated as the surface area measured with 0.16 mm mesh size and divided by the projected area. The fractal dimension was defined by the grid scaling method (Mechtcherine et al. 1995).

This method is based on the fact that the measured surface area increases as the grid size decreases. The plot of the logarithm (ln) of the measured surface area (here related to projection area) over the logarithm of the grid size gives the negative value of fractal increment = *tan α* (Figure 6). The grid scaling fractal dimension D_{GS} can be calculated by adding this value to the dimension of a plane = 2.

Table 3 gives the results of the calculations. The roughness and the fractal dimension of the fracture surface increase with decreasing strength of con-
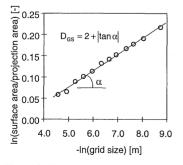

Figure 6. Plot based on the grid scaling method applied to characterize the fracture surface of a typical concrete specimen

crete. The fracture surfaces of the unsealed normal strength concrete are rougher than those of the sealed NSC.

Table 3. Roughness and fractal dimension of concrete fracture surfaces of the concretes under investigation

Concrete	Roughness R_S	Fractal Dimension D_{GS}
HSC, sealed	1.167 (0.008)	2.029 (0.001)
NSC, sealed	1.258 (0.013)	2.044 (0.003)
NSC, unsealed	1.323 (0.040)	2.052 (0.003)

Standard deviations are given in parentheses.

The roughness R_S of the components of fracture surfaces was derived from the surface area measured with 1.252 μm mesh size. Also in this case the grid scaling method was applied to calculate the fractal dimension.

According to Table 4 the micro-roughness and fractal dimension of the fractured cement paste of the HSC are lower than the corresponding values of the NSC. The fractured cement paste of the unsealed NSC has the roughest surface. Also the cement paste-aggregate interface of the unsealed NSC is rougher than that of the sealed NSC. The fractured aggregates of the high-strength concrete provided rather strongly varying R_S- and D_{GS}-values. This was caused by a significant variation of the microstructure of the aggregate grains investigated.

Table 4. Roughness and fractal dimension of the fracture surfaces of the concrete components

Concrete	Components	Roughness R_S [-]	Fractal Dimension D_{GS} [-]
HSC, sealed	Cement paste	1.636 (0.239)	2.087 (0.027)
	Fract. aggregate	1.238 - 2.368	2.047 - 2.184
NSC, sealed	Cement paste	1.718 (0.047)	2.097 (0.016)
	CP/Agg.-Interface	1.465 (0.137)	2.080 (0.019)
NSC, unsealed	Cement paste	1.940 (0.159)	2.119 (0.011)
	CP/Agg.-Interface	1.782 (0.147)	2.111 (0.011)

Standard deviations are given in parentheses.

4 DISCUSSION OF THE EXPERIMENTAL RESULTS

With increasing strength of concrete an increase of the strain ε_{tu} was observed (Tab. 2 and Fig. 7, above). Drying of the normal strength concrete had no significant effect on this material parameter. However, considering only the non-linear deformation component of the strain $\varepsilon_{tu,nl}$ ($\varepsilon_{tu,nl} = \varepsilon_{tu} - f_t/E_0$) the highest values are obtained for the unsealed NSC and the lowest ones for the HSC. The σ-ε relation of the NSC is more non-
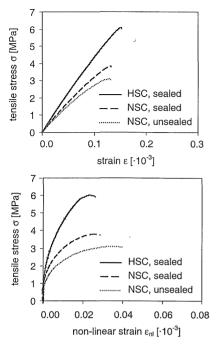
Figure 7. Measured σ-ε-relations (above) and calculated non-linear strains ε_{nl} on different stress levels (below) for the normal strength and the high-strength concretes

linear than that of the HSC due to the advanced micro-cracking which is observed for the NSC. Figure 7 (below) shows calculated non-linear strains ε_{nl} ($\varepsilon_{nl}= \varepsilon - \sigma/E_0$), i.e. strains caused by micro-cracking. The unsealed NSC provided the most pronounced non-linearity.

These results are in agreement with the observations of the development of microcracks in a normal strength and a high-strength concrete under compression using X-Ray technique (Smady & Slate 1989). Further, the non-linear strains, which represent a measure of the damage in concrete due to micro-cracking, correlate to the values of the roughness R_S and the fractal dimension D_{GS} detected for the components of the fracture concrete surfaces on the microlevel (refer to Tab. 4). It appears to be a consistent result, that the pronounced micro-cracking for the NSC has to cause a rougher failure surface.

The uniaxial tension tests provided for the high-strength concrete approximately 20 % higher values of the fracture energy than the corresponding values of the sealed normal strength concrete. However, for the unsealed NSC a slightly higher G_F-value has been found than for the HSC. The predicted effect of the concrete strength on the fracture energy of concrete according to Model Code 1990 (CEB-FIP 1993) is much higher: for the two investigated concretes an

increase of 80 % is obtained. One reason may be, that the former experiments to determine the fracture energy were performed up to relatively small deformations. In this case, mainly the first steeper part of the descending branch of the stress-deformation relation could be recorded.

Figure 8 shows the influence of the concrete strength and the curing conditions on the shape of the stress-deformation relation. For the HSC the area under the initial part of the σ-δ relation is larger than that for the NSC, because of a higher tensile strength and higher values for δ_{tu}. This indicates an increase of energy consumption for the formation and propagation of narrow cracks with increasing strength of concrete. For larger crack widths this trend reverses, and the σ-δ relations for the NSC are above those for the HSC. This difference is small in the case of the sealed NSC, but it is significant in the case of the unsealed NSC. The condition of the fracture surfaces gives an explanation for this phenomenon: the higher roughness and the higher fractal dimensions of the fracture surfaces of the NSC, especially of the unsealed ones (see Tab. 3) indicate a pronounced crack surface interlocking, which provides a better transfer of the tensile stresses across the crack.
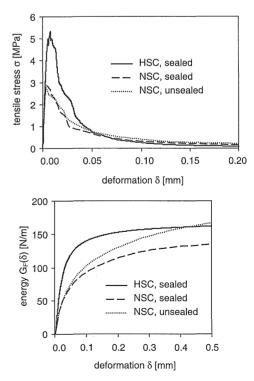

Figure 8. Influence of the concrete strength and the curing conditions on the shape of the σ-δ relation (above) and on the energy consumption due to the fracture process (below)

5 NUMERICAL MODELLING

5.1 *Generation of fracture surfaces*

The values of the fractal dimension obtained from the fractological investigations can be used as input data for the generation of the artificial fracture surfaces. This approach was initially used for the estimation of the reliability of the values derived from fractological measurements (Mechtcherine & Müller 1999). In this study, this method was applied for the generation of FE meshes for a numerical analysis of concrete failure.

For the generation of the artificial fracture surfaces the midpoint displacement method was applied, which had been initially developed for the simulation of Brownian motion (Peitgen & Saupe 1988). Figure 9 shows schematically the first four steps in applying the one-dimensional version of the midpoint displacement method. In the first step a straight line is generated, which one end has a zero altitude while the other end is defined as a sample of a Gaussian random variable A_0 with a mean value of zero and unit variance σ^2. In the next step the midpoint between these two end points is calculated and displaced by a random variable A_1 with a mean value of zero and variance $(\Delta_1)^2$. Further, new midpoints between the neighboring points are considered and displaced by a random value A_2, which is in average smaller than the displacements in the former steps.

The procedure can be continued until the desired resolution is achieved. The variances of the displacement variables are calculated using Equation 1, where n is the step number and H is the Hust exponent depending on the chosen fractal dimension:

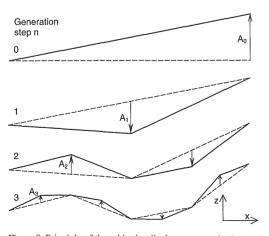$$\Delta_n^2 = \frac{\sigma^2}{(2^n)^{2H}}(1 - 2^{2H-2}) \tag{1}$$

Figure 9. Principle of the midpoint displacement method

where $H = 2 - D_L$ and D_L = fractal dimension of a line, i.e. the crack profile.

A similar procedure was applied for the generation of fracture surfaces. In this case for the calculation of the altitude of each midpoint four neighboring points in a quadratic lattice were used. The displacement variances $(\Delta_1)^2$ were derived using Equation 2 governed by the fractal dimension of a surface D_S. Details may be found in Mechtcherine 2000.

$$\Delta_n^2 = \sigma^2 (\tfrac{1}{2})^{n(3-D_S)} \tag{2}$$

Figure 10 shows typical crack profiles obtained from the fracture surfaces generated using different fractal dimensions. The profile taken from the artificial surface with a fractal dimension $D_S = 2.05$, which approximately corresponds to the values obtained by the authors in the fractological investigations, looks rather similar to those optically measured for the high-strength concrete. The crack profiles having a considerably higher fractal dimension appear less realistic.
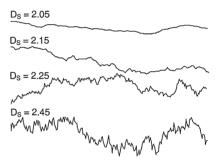
Figure 10. Typical crack profiles of generated fracture surfaces

Figure 12 (above) shows an artificial surface, which was generated using a fractal dimension $D = 2.03$ (which corresponds approx. to the average D_{GS}-value obtained in the fractological investigations for the concrete HSC, see Tab. 3). Since the artificial fracture surface (Fig. 12, above) looks similar to the measured fracture surfaces of the high-strength concrete (Fig. 2, above), the midpoint displacement method seems to be quite good for the generation of fracture surfaces with dominating aggregate failure (besides high-strength concrete this is typical e.g. for lightweight aggregate concrete too). To simulate the fracture surfaces of ordinary concretes the generated surfaces have to be accomplished by some portion of unbroken aggregates.

For this purpose the "crater and hill"-method was developed on the basis of a similar technique applied for the generation of "moon landscapes" (Scholl & Pfeiffer 1991). In this method first a point on a generated fracture surface is randomly chosen. Figure
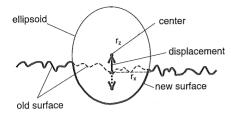
Figure 11. "Crater and hill"-method

11 shows a corresponding crack profile as a sectional view of the surface in the x-z plane. In the next step this point is displaced up or down, again randomly. From now on the displaced point serves as the center of an ellipsoid with random radii r_x, r_y and r_z which are linked to the minimum and maximum aggregate size. In the following step the z-coordinates of the concerned lattice points are redefined to reproduce the shape of a "crater" or a "hill", depending on the position of the ellipsoid center with respect to the surface plane. The procedure has to be repeated so many times until the surface is provided with the desired amount of unbroken aggregates.
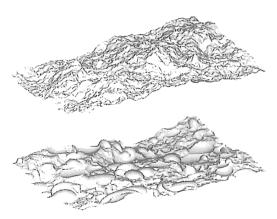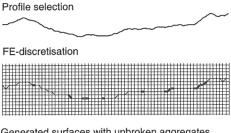

Figure 12. Example of artificial surfaces with "broken" (above) and "unbroken aggregates" (below)

Figure 12 (below) gives an example of an artificial surface with a high content of "unbroken aggregates". The calculation of the fractal dimension of the generated fracture surfaces with and without "aggregate fracture" showed that the "addition" of the unbroken aggregates to the generated surfaces increased the D_{GS}-value from initially $D_{GS} = 2.03$ up to approx. $D_{GS} = 2.06$. Therefore, by means of the "crater and hill"-method the effect of the unbroken aggregate on the condition of the failure surfaces, which was observed experimentally, could be properly modelled for artificial fracture surfaces.

5.2 Numerical analysis

The generation of fracture surfaces or crack profiles is a powerful tool for a comprehensive analysis of different physical and mechanical phenomena with regard to concrete cracking (Mechtcherine 2000). In this study the artificial fracture surfaces were used for modeling the mesh in a FE analysis in order to investigate the transmission of stresses across discrete cracks in concretes with and without aggregate failure.

Figure 13. Application of crack profiles in a FE analysis

First a profile of a generated surface with "complete aggregate failure" was selected (Fig. 13, above). After having added some "craters" and "hills" to the surface a new profile of the same section was chosen again (Fig. 13, middle). Then both profiles were discretized using interface elements. Finally, the properties of the concrete components, i.e. mortar, coarse aggregate and bond were assigned to the corresponding finite elements. For this purpose both discretized profiles were compared. The common elements represented the mortar matrix. Other elements were considered to belong to the aggregates in the case of the first profile and to the bond zone in the case of the second profile (Fig. 13, below).

Table 5. Input parameters for the components of the concrete fracture surfaces

Input pa-rameter	E_0 [GPa]	$f_{t,mortar}$ [MPa]	$G_{F,mortar}$ [N/m]	$f_{t,agg}$ [MPa]	$G_{F,agg}$ [N/m]	$f_{t,bond}$ [MPa]	$G_{F,bond}$ [N/m]
model 1a	35	4	60	4	60	-	-
model 2a	35	4	60	-	-	4	60
model 1b	45	7	70	7	100	-	-
model 2b	35	6	60	-	-	2	60

In the first series of calculations exactly the same fracture mechanical properties, i.e. tensile strength f_t and fracture energy G_F were assigned to all elements, see Table 5, models 1a and 2a. As a result, only the effect of the crack geometry could be studied. In the analysis a linear stress-crack opening relation was assumed. The comparison of the calculated σ-δ relations shows that the model with unbroken aggregates provided a better stress transfer across the crack than the model with aggregate failure, see Figure 14 (left).
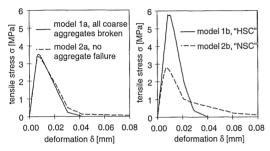

Figure 14. Effect of the crack profile geometry (left) and of the properties of the concrete components (right) on the shape of the calculated stress-deformation relations

The difference becomes much more evident if more realistic values of the tensile strength and the fracture energy for the concrete components are used, see Table 5. In this calculation series model 1b was considered to represent high-strength concrete and model 2b normal strength concrete, respectively. As a result, the obtained σ-δ relations for both concretes showed a reasonably good agreement with the corresponding curves from the experiments for small as well as for large crack openings, compare Figures 8 (above) and 14 (right).

4 SUMMARY AND CONCLUSIONS

The investigated high-strength concrete has a higher strain ε_{tu} at tensile strength f_t, and when approaching the tensile strength, it has a lower value of the non-linear strain $\varepsilon_{tu,nl}$ than a normal strength concrete. The strongest non-linearity of the σ-ε relation, indicating the most advanced micro-cracking, was observed for the unsealed normal strength concrete. These observations correlate well with the results from the optical measurements of the micro-roughness of the fracture surfaces: the high-strength concrete provided the lowest and the unsealed normal strength concrete the highest values of the micro-roughness R_S and the fractal dimension D_{GS} on the microlevel.

The higher roughness R_S and the higher fractal dimension D_{GS} of the entire fracture surfaces of the NSC, especially of the unsealed one, indicate a better transfer of tensile stress across the crack. This results in a less steep descending branch of the σ-δ relation and in a higher energy consumption at larger crack widths in comparison to the high-strength concrete.

The generation of fracture surfaces was applied for the FE analysis of mechanisms of the stress transfer over discrete cracks. The results of the FE simulations confirmed the experimentally found correlations between the condition of the failure surface and the fracture mechanical properties of the investigated concretes.

5 REFERENCES

CEB-FIP Model Code 1990, *CEB Buletin D'Information* 213/214, Lausanne.
Mechtcherine, V. 2000. *Investigations on crack spreading in concrete.* Doctoral thesis, University of Karlsruhe, in German.
Mechtcherine, V., Garrecht, H. & Hilsdorf, H.K. 1995. Effect of temperature and loading rate on fracture behaviour of concrete subjected to uniaxial tension. In F.H. Wittmann (ed.), *Fracture Mechanics of Concrete Structures*: 719-728. Freiburg: Aedificatio Publishers.
Mechtcherine, V., Müller, H. S. 1999. Fractological and numerical investigations on the fracture mechanical behaviour of concrete. F. H. Wittmann (ed.), *Proceeding of EURO-MAT 99*, 6: 119-124. Weinheim: Wiley-VCH.
Mihashi, H., Nomura, N., Umeoka, T. 1994. *Fracture mechanics parameters of cementitious composite materials and fractured surface properties.* Europe - U.S. Workshop on Fracture and Damage in Quasibrittle Structures, Prague
Peitgen, H.-O., Saupe, D. 1988. *The Science of Fractal Images*, New York: Springer-Verlag.
Scholl, R., Pfeiffer, O. 1991. *Natur als fraktale Grafik.* München: Markt&Technik Verlag
Smadi, M. M., Slate, F. O. 1989. Microcracking of high and normal strength concretes under short- and long-term loadings. *ACI Materials Journal* 86 (2): 117-127.
Wilson, T. 1990. *Confocal microscopy.* London: Academic Press Ltd.
Wolf, Th., Gutmann, B., Weber, H. 1996. Fuzzi logic - a new tool for 3-D displacement measurements. *International Society for Optical Engineering, SPIE-Proceedings* 2782: 363-375.